

**Atomic corrugation and electron localization due to Moiré patterns in twisted bilayer graphenes**Kazuyuki Uchida,<sup>\*</sup> Shinnosuke Furuya,<sup>†</sup> Jun-Ichi Iwata, and Atsushi Oshiyama*Department of Applied Physics, The University of Tokyo, Tokyo 113-8656, Japan*

(Received 5 March 2014; revised manuscript received 2 October 2014; published 28 October 2014)

We report on unprecedentedly large-scale density-functional calculations that clarify atomic and electronic structures of twisted bilayer graphene (BLG). We find the existence of the critical twist angle from either the AB or the AA stacking BLG, above which the two graphene layers are essentially decoupled and below which the atomic planes are corrugated and the Dirac electrons are localized. We also find a magic angle at which the Fermi velocity of the Dirac electron vanishes. We clarify that the Moiré pattern in tBLG with a tiny twist angle generates inhomogeneity for the electron systems and thus causes the drastic modification of the electronic properties, leading to flat bands at the Fermi level. Sensitivity to the Moiré of the valence-electron density and the electron state near the Fermi level is discussed.

DOI: [10.1103/PhysRevB.90.155451](https://doi.org/10.1103/PhysRevB.90.155451)

PACS number(s): 61.48.Gh, 73.22.Pr, 74.20.Pq

**I. INTRODUCTION**

Interference of two waves causes rich phenomena in nature. Beat patterns in sounds and Moiré patterns in sights are commonly recognized in human life. In condensed matter, two periodicities in atomic arrangements slightly different from each other induce a Moiré pattern: e.g., turbostratic stacking of surface layers of graphite leads to a Moiré pattern which is observed by scanning tunneling microscope (STM) [1,2]. How electron waves sense Moiré patterns of atomic arrangements is an intriguing issue. In this paper, we clarify the decisive role of Moiré in the atomic structures and electron states of twisted bilayer graphene (tBLG) [3].

Bilayer graphene (BLG) is produced by exfoliation of graphite [4,5] or by heat treatments of SiC surfaces [6,7]. Typical stacking of the two layers is either AB (Bernal) or AA. However, the two graphene layers are often twisted to each other in their basal planes. The layers with a tiny twist angle  $\theta$  generate a Moiré pattern with its period  $L = \sqrt{3}d/(2 \sin \frac{\theta}{2})$ , where  $d$  is the C-C bond length [4–10].

The electronic structure of tBLG, in particular the behavior of Dirac electrons [11,12], has been intensely debated: Raman spectra [5], STM images [7], ARPES data [13], and theoretical calculations [6,14,15] indicate decoupling of twisted layers, leading to linear-dispersive Dirac electrons as those in single-layer graphene (SLG). On the other hand, another Raman spectra [4], effective Hamiltonian theory [16,17], and tight-binding calculations [17–19] indicate substantial reduction of the Fermi velocity  $v_F$  in tBLGs with small twist angles  $\theta$ . This  $v_F$  reduction for small  $\theta$  is also supported by a Landau-level spectroscopy combined with STM [8]. No such reduction, however, is deduced from ARPES experiments [9,10]. In addition, existence of the interesting magic angle  $\theta_M$  at which  $v_F$  vanishes is predicted using the continuum theory [20]. To exploit fascinating properties of graphene in device applications, it is important to resolve these issues.

It is thus highly demanded to perform reliable first-principles calculations for tBLGs systematically. However, even if we confine ourselves to tBLGs where the Moiré period  $L$  is commensurate with that of SLG, first-principles

calculations have been regarded as formidable since the number of atoms in a unit cell increases tremendously with decreasing  $\theta$ , reaching tens of thousands for  $\theta \leq 1^\circ$ . We here apply our real-space scheme (RSDFT code) [21] which has been optimized for current massively parallel supercomputers and enables us to perform the total-energy electronic-structure calculations for unprecedentedly large systems consisting of 10–100 thousand atoms [22] in the density-functional theory (DFT) [23,24].

We find that there is a critical twist angle  $\theta_c \sim 5^\circ$  from either the AA or AB stacking, below which the Fermi velocity  $v_F$  decreases dramatically toward zero to cause flat bands at the Fermi level  $E_F$ . This  $v_F$  reduction is a consequence of localization of electrons sensing the Moiré in tBLGs. We discover a magic angle  $\theta_M \sim 1.08^\circ$  where  $v_F$  vanishes. We also find that the two graphene layers are corrugated below another critical angle  $\theta_a \sim 10^\circ$ . The two critical angles  $\theta_c$  and  $\theta_a$  are *unequal* to each other, reflecting the difference in the sensitivity to the Moiré between the electron waves near  $E_F$  and the valence-electron density in the honeycomb lattice which decides the atomic structure.

The organization of this paper is as follows. Our calculational method is briefly described in Sec. II, and its details are given in the Appendix. Section III presents our systematic results on the atomic and electronic structures of tBLGs for various twist angles. Section IV summarizes our findings.

**II. METHOD**

Calculations have been performed using the local-density approximation (LDA) [25] to the exchange-correlation energy in the DFT. Ultrasoft pseudopotentials [26] are used to describe the electron-ion interactions. We have examined 58 commensurate tBLGs with various twist angles including the smallest  $\theta = 0.76^\circ$  (22 708 atoms per cell). Details of the present calculations are in Appendix A. We have also examined the validity of LDA by repeating the calculations using van der Waals (vdW)-DFT functional [27]. The results obtained are essentially identical to those by LDA (Appendix E).

**III. RESULTS**

We set out structural optimizations. Figure 1 shows tBLGs for three representative twist angles  $\theta$ . For  $\theta = 29.4^\circ$ , the two

<sup>\*</sup>kuchida@ap.t.u-tokyo.ac.jp<sup>†</sup>Present address: Argo Graphics Inc., Tokyo 103-0015, Japan.

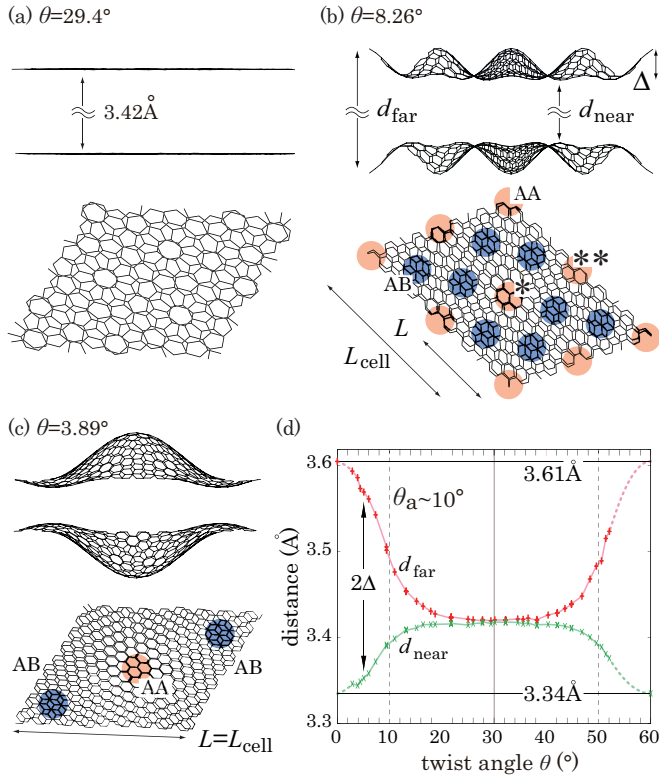


FIG. 1. (Color online) The side and top views of the optimized tBLG with the twist angle  $\theta$  of (a) 29.4°, (b) 8.26°, and (c) 3.89°. In (b) and (c), the corrugation  $\Delta$  is visible with the longest distance  $d_{\text{far}}$  and the shortest distance  $d_{\text{near}}$ . In (d),  $d_{\text{far}}$  and  $d_{\text{near}}$  as functions of the twist angle  $\theta$  are shown. The crosses are the calculated values. The lines are guides for eyes. The orange (light) and blue (dark) circles in (b) and (c) depict the AA and AB stacking regions, respectively.

layers are almost flat [Fig. 1(a)] with the interlayer distance of 3.42 Å. This value is between the distances in the AA stacking ( $\theta = 0^\circ$ ) and the AB stacking ( $\theta = 60^\circ$ ) BLGs, which are  $d_{\text{AA}} = 3.61$  Å and  $d_{\text{AB}} = 3.34$  Å, respectively, in our LDA calculations. When  $\theta$  becomes small, we observe Moiré patterns in which the AA and AB stacking regions as well as other stacking regions constitute a patchwork:  $\theta = 8.26^\circ$  and  $3.89^\circ$  in Figs. 1(b) and 1(c), respectively (see also Appendix B and Fig. 7). The period  $L$  of the patchwork pattern and the size of each of the AA and AB stacking regions increase as  $\theta$  becomes close to  $0^\circ$  (or  $60^\circ$ ) [Fig. 7 in the Appendix]. For small  $\theta$ , the two layers are corrugated. The interlayer distance is the longest ( $d_{\text{far}}$ ) in the AA stacking region and the shortest ( $d_{\text{near}}$ ) in the AB stacking region. The calculated amounts of the corrugation,  $\Delta \equiv (d_{\text{far}} - d_{\text{near}})/2$ , are 0.07 Å and 0.12 Å for  $\theta = 8.26^\circ$  and  $3.89^\circ$ , respectively. The corrugation is periodic. Its period is identical to that of the Moiré:  $L = 16.96$  Å and  $35.98$  Å for  $\theta = 8.26^\circ$  and  $3.89^\circ$ , respectively.

Period of the supercell  $L_{\text{cell}}$  is not necessarily identical to the Moiré period  $L$ : e.g., for  $\theta = 8.26^\circ$ ,  $L$  is a half of  $L_{\text{cell}}$  [Fig. 1(b)]. Interestingly, though the atomic structures in the regions marked by \* and \*\* in the top view of Fig. 1(b) are different, the amount of the corrugation is essentially the same for the regions. This indicates that what is relevant to the corrugation is the Moiré pattern, *not* the detailed atomic structure.

Figure 1(d) summarizes the corrugation of the calculated tBLGs as a function of the twist angle  $\theta$ . The upper and lower curves show the longest ( $d_{\text{far}}$ ) and the shortest ( $d_{\text{near}}$ ) interlayer distances, respectively. We have found that the amount of the corrugation is a unique function of  $\theta$  (and thus of the Moiré period  $L$ ), but that the behavior is peculiar: In the range of  $20^\circ < \theta < 40^\circ$ , the corrugation is *absent*; when  $\theta < 20^\circ$  or  $> 40^\circ$ , the corrugation begins and the  $d_{\text{far}}$  and  $d_{\text{near}}$  approach to  $d_{\text{AA}}$  and  $d_{\text{AB}}$ , respectively; for  $\theta = 0^\circ$  or  $60^\circ$ , the corrugation is absent again. The results reveal the existence of a critical twist angle  $\theta_a$  below which the corrugation is prominent. Figure 1(d) indicates that  $\theta_a$  is about  $10^\circ$ .

The critical twist angle of  $\theta_a \sim 10^\circ$  corresponds to the Moiré period of  $L \sim 10d$ . This assures the extent of the AA stacking region being  $\sim 3.3a_0$  (see Appendix C), where  $a_0 = \sqrt{3}d$  is the lattice constant of the honeycomb lattice. It is thus concluded that atoms on the honeycomb lattice, in other words the valence electron density, sense the Moiré when it causes a locally distinct region of the size. In Fig. 1(d), the calculated distances of tBLGs with largely different  $L_{\text{cell}}$  but with similar  $\theta$  are compiled as a unique function of  $\theta$ . This strongly infers that the present results for the atomic corrugation obtained for the commensurate tBLGs are *not* owing to the periodicity  $L_{\text{cell}}$  imposed *but* applicable even to the incommensurate tBLGs. The corrugation we have identified is indeed observed in the STM images [6–8,10].

A tBLG with  $\theta \rightarrow 0^\circ$  and a BLG with  $\theta = 0^\circ$  are qualitatively different: The former shows Moiré pattern, while the latter does not; the corrugation is prominent with  $d_{\text{far}} \rightarrow 3.61$  Å and  $d_{\text{near}} \rightarrow 3.34$  Å in the former, while it is absent with a unique interlayer distance of 3.61 Å in the latter. The twist angle  $\theta = 0^\circ$  is a singular point. Such singularity is also observed at  $\theta = 60^\circ$ .

Figure 2 shows the calculated binding energy of tBLG defined as  $E_b = (2E_{\text{gra}} - E_{\text{tBLG}})/N$  as a function of  $\theta$ , where  $N$  is the number of C atoms per cell, and  $E_{\text{gra}}$  and  $E_{\text{tBLG}}$  are the total energies of SLG and tBLG, respectively. We have found that  $E_b$  is almost constant with the variance of a few % in the range of  $0^\circ < \theta < 60^\circ$ , although there is a shallow minimum around  $\theta = 30^\circ$ . This is a reason why STM experiments show various images with different Moiré patterns. The singularity at  $\theta = 0^\circ$  and  $60^\circ$  mentioned above manifests itself in the binding energy. The calculated  $E_b$  remains almost constant even to  $\theta \rightarrow 0^\circ$  and  $\theta \rightarrow 60^\circ$ , and abruptly jumps to the corresponding values of  $E_b$ , 7.0 meV/atom ( $\theta = 0^\circ$ ) and 11.9 meV/atom ( $\theta = 60^\circ$ ) (Fig. 2). This discontinuity is peculiar to infinite-size tBLGs.

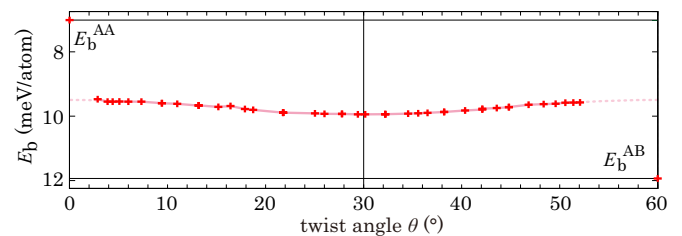


FIG. 2. (Color online) Binding energy  $E_b$  per atom as a function of  $\theta$ . The crosses show calculated values. The line is a guide for eyes.

When the lateral size is finite, this discontinuity generally disappears. Suppose a finite-size AA or AB stacking BLG with a particular shape. When the two layers are twisted slightly from  $\theta = 0^\circ$  ( $60^\circ$ ), the stacking is almost AA (AB). This makes the  $E_b$  curve steep but continuous near  $\theta = 0^\circ$  and  $60^\circ$ . The nearly constant behavior of  $E_b$  is also modified in the finite-size tBLGs. The energetically favorable twist angles are expected since the ratio of the most stable stacking region to the less stable stacking regions varies with the twist-angle variation. This is actually found in the previous calculations for bilayer graphene flakes [28,29].

In Figs. 1(d) and 2, we observe that the corrugation  $\Delta(\theta)$  and the binding energy  $E_b(\theta)$  are almost symmetric with respect to  $\theta = 30^\circ$ . The structure with  $60^\circ - \theta$  is obtained from that with  $\theta$  by translating one layer with respect to the other after a mirror inversion of the system. Since the mirror inversion does not change energetics, the essential difference between the two structures is the lateral translation. The observed symmetry with respect to  $\theta = 30^\circ$  indicates that the translation has minor effects. We therefore safely confine ourselves to the range of  $0^\circ < \theta < 30^\circ$  hereafter.

We are now in a position to discuss the electronic structure of tBLG. Figure 3 shows the calculated energy bands of three representative tBLGs. For the twist angle of  $\theta = 29.4^\circ$ , we have found energy bands with the linear dispersion near the Fermi level  $E_F$  as in SLG [Fig. 3(a)]. In tBLG, the linear band near  $E_F$  is almost doubly degenerate, leading to fourfold degenerate states at the K point. The Fermi velocity  $v_F \equiv (\partial\varepsilon/\partial k)/\hbar$  of this Dirac electron is essentially identical

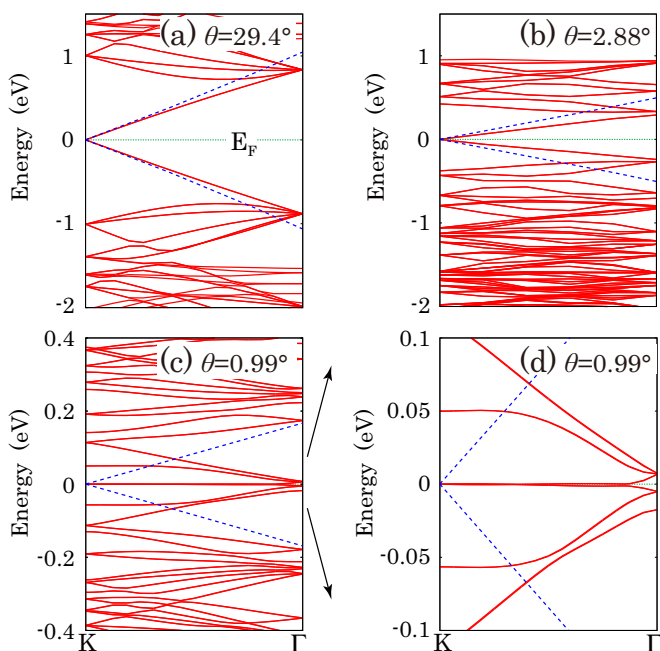


FIG. 3. (Color online) Energy bands of tBLGs with  $\theta = 29.4^\circ$  (a),  $2.88^\circ$  (b), and  $0.99^\circ$  (c). The Fermi level  $E_F$  is set to be 0. The enlargement near  $E_F$  for  $\theta = 0.99^\circ$  is shown in (d). The energy scale is different in each figure. Also the size of the Brillouin zone is different since the numbers of the atoms in each (hexagonal) unit cell are 388 (a), 1588 (b), and 13 468 (c),(d), respectively. The Dirac bands of a SLG are also shown by blue (dashed) lines.

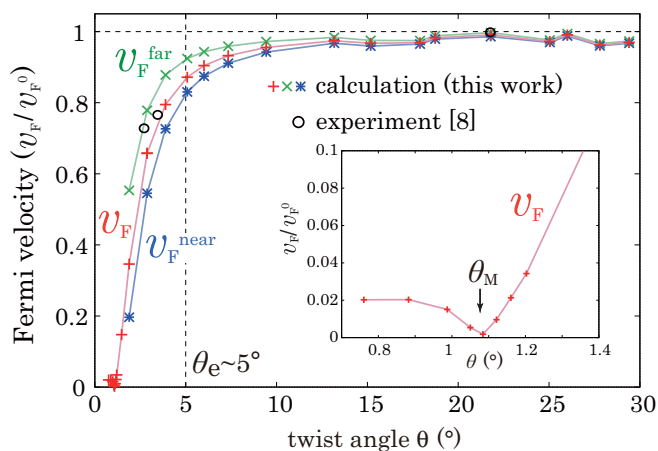


FIG. 4. (Color online) Fermi velocity normalized to that of SLG  $v_F^0$ , as a function of  $\theta$ : the velocities in the optimized structures ( $v_F$ ); those for the flat structures with the interlayer distances of  $3.61 \text{ \AA}$  ( $v_F^{\text{far}}$ ) and  $3.34 \text{ \AA}$  ( $v_F^{\text{near}}$ ). Black circles are experimental data [8].

to that of SLG  $v_F^0$ . This corresponds to the decoupling of the two layers argued previously [5–7,13–15]. However, when  $\theta$  decreases,  $v_F$  is reduced substantially. For  $\theta = 2.88^\circ$ ,  $v_F$  is  $\sim 0.66v_F^0$  [Fig. 3(b)]. This reduction is in accord with the previous works based on the experiments [8] and the empirical calculations [16–19].

When  $\theta$  is as small as  $0.99^\circ$ , the energy bands show a dramatic variation [Figs. 3(c) and 3(d)]: The bands near  $E_F$  become flat in most of the Brillouin zone, indicating that  $v_F$  approaches to zero. The flat bands are half filled, inferring that the magnetic behavior occurs by slightly twisting BLG. Interestingly, at the  $\Gamma$  point, the flat bands split with the energy gap of 10 meV. It is of interest to clarify the relation between the Fermi-velocity reduction at the K point, the flatness of the corresponding band, and the energy gap at the  $\Gamma$  point.

The variation of  $v_F$  as a function of  $\theta$  is shown in Fig. 4. We have found that  $v_F$  is almost the same as that in SLG for  $\theta > 10^\circ$ , and that it is dramatically reduced toward zero when  $\theta < \theta_c$ . Figure 4 shows that the critical angle  $\theta_c$  is about  $5^\circ$ . The calculated velocity for the optimized structure  $v_F$  agrees well with the experimental values obtained by Landau-level spectroscopy for  $\theta \sim 3^\circ$  [8]. However, there may be a reason to be clarified why the ARPES experiments observe no reduction of  $v_F$  [9,10]. We have also calculated the Fermi velocity of flat tBLGs with the interlayer distance in the AA stacking BLG ( $3.61 \text{ \AA}$ ),  $v_F^{\text{far}}$ , and that in the AB stacking BLG ( $3.34 \text{ \AA}$ ),  $v_F^{\text{near}}$ . It is found that the geometry optimization is imperative to assess the amount of the  $v_F$  reduction quantitatively, yet the existence of the critical twist angle  $\theta_c$  is common to all cases.

The reason for the reduction of  $v_F$  and then the emergence of the flat bands is ascribed to the electron localization due to the Moiré pattern. Figure 5 shows Kohn-Sham orbitals at  $E_F$  for two representative tBLGs. For  $\theta = 29.4^\circ$ , the Kohn-Sham orbitals are characterized by  $\pi$  orbitals extending over the whole region [Fig. 5(a)]. However, when  $\theta$  becomes as small as  $0.99^\circ$  [Fig. 5(b)], the Moiré pattern becomes prominent and the Kohn-Sham orbitals at  $E_F$  are localized in the AA stacking region. The localization is also found for other states, though the region and amount of the localization depends on

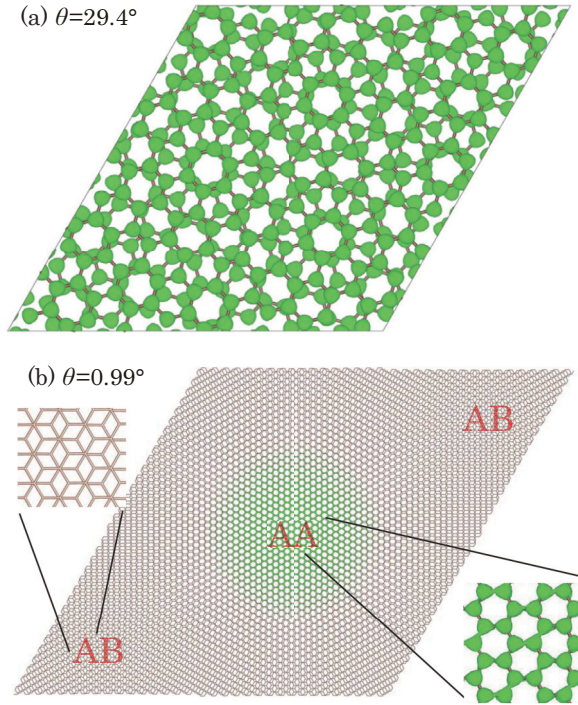


FIG. 5. (Color online) The squared Kohn-Sham orbitals at the Fermi level  $E_F$ , summed over fourfold degenerate states. The  $\theta$  is (a)  $29.4^\circ$  and (b)  $0.99^\circ$ . The AA and AB in (b) depict the local AA and AB stacking regions, respectively.

band index and  $k$  point. The Moiré pattern which becomes prominent for small  $\theta$  induces inhomogeneity. The electron wave senses the inhomogeneity, and finally the Kohn-Sham orbitals are localized.

The reduction in  $v_F$  is not monotonic, however. As shown in the inset of Fig. 4,  $v_F$  vanishes at  $\theta_M \sim 1.08^\circ$  and then slightly increases for the smaller  $\theta$ . There is a magic angle  $\theta_M$  at which  $v_F$  vanishes. This behavior is consistent with previous arguments by a continuum model [20] and a tight-binding calculation [30]. Yet, the present value differs from those by the empirical methods:  $1.05^\circ$  [20] and  $1.13^\circ$  [30]. We have unequivocally shown the existence of the magic angle in real geometry optimized tBLGs.

The existence of the critical angle  $\theta_c$  in Fig. 4 is a manifestation of the sensitivity to the Moiré pattern of the electron wave at  $E_F$ . The critical angle  $\theta_c \sim 5^\circ$  corresponds to the Moiré period  $L \sim 20d$ . This assures the extent of the AA-stacking region being  $\sim 6.6a_0$  (see Appendix C). This size is necessary to make the electron at  $E_F$  sense the Moiré. When the interlayer interaction becomes stronger as in  $v_F^{\text{near}}$ , the critical angle  $\theta_c$  is unchanged though the  $v_F$  reduction is enhanced, supporting our argument that the Moiré pattern with the critical size of the AA stacking region is essential. It is intriguing that the critical angle for the electron localization  $\theta_e$  ( $\sim 5^\circ$ ) is a half of the critical angle for the structural corrugation  $\theta_a$  ( $\sim 10^\circ$ ) already discussed [Fig. 1(d)]: The density of all valence electrons, which plays a decisive role in the structural corrugation, senses the Moiré pattern with larger twist angle (smaller AA stacking region). This may be a reflection of general statement that the density matrix represented in real space is more localized than the electron orbital of each state [31].

#### IV. CONCLUSION

In summary, we have performed unprecedentedly large-scale density-functional calculations in our real-space scheme for tBLGs. We have shown that the graphene layers in tBLG are essentially decoupled for the twist angle  $\theta \sim 30^\circ$  and are strongly coupled to each other for  $\theta$  close to  $0^\circ$  and  $60^\circ$ . Two regimes are separated by the critical angle  $\theta_a$  ( $\sim 10^\circ$ ,  $50^\circ$ ) for atomic structures and  $\theta_e$  ( $\sim 5^\circ$ ,  $55^\circ$ ) for electron states. The small twist from the AA or AB stacking BLG causes atomic corrugation of the layers and also the drastic reduction in the Fermi velocity  $v_F$ , eventually leading to the emergence of the half-filled flat bands at the Fermi level with  $\theta \sim 1^\circ$ . We have also shown the magic twist angle  $\theta_M \sim 1.08^\circ$  where  $v_F$  vanishes.

#### ACKNOWLEDGMENTS

This work was supported by the Grants-in-Aid for scientific research under the Contract No. 22104005 and the CMSI project, both conducted by MEXT, Japan. Computations were performed mainly at the K computer, Kobe and Supercomputer Center in ISSP, The University of Tokyo, Japan.

#### APPENDIX A: REAL-SPACE DENSITY-FUNCTIONAL CALCULATIONS

Architecture of current and future supercomputers is rapidly changing. The current TOP 10 supercomputers are mostly of the multi-core massively parallel architecture [32], and in future many-core and/or hardware-accelerated architecture is expected to emerge. In this circumstance, the development of new schemes of the calculations associated with suitable algorithms is imperative.

To perform accurate large-scale total-energy electronic-structure calculations efficiently on the current and future architectures, we have adopted a real-space (RS) scheme [33,34] in the density functional theory (DFT) combined with the first-principles pseudopotential method, and have developed a highly efficient computation code named RSDFT [21]. In the real-space scheme, discrete grid points are introduced in real space, and the Hamiltonian in the Kohn-Sham (KS) equation in the DFT is expressed as a matrix represented at the grid-point space. Differential operators for kinetic energy are replaced by finite-difference operators with sufficiently high orders. Hence, the Hamiltonian matrix becomes sparse and fast-Fourier transformation (FFT) is not required for the Hamiltonian operation. FFT generally causes heavy communication burden among all the compute nodes in the conventional plane-wave basis-set scheme. As a result, the communication in the RSDFT code arises from the finite-difference operations, the nonlocal pseudopotential operations, and the nonlocal exchange-correlation functional operations, if any. Hence, the communication becomes local only among neighboring compute nodes, so that the total communication cost is tremendously reduced. In fact, the RSDFT shows good scalability even with 80 000 compute nodes at K computer at Kobe, Japan [35].

The basic algorithm to solve KS equation is almost the same as that used in the conventional  $O(N^3)$  scaling method. The main routines are constructed from three parts:

conjugate-gradient minimization, Gram-Schmidt orthonormalization, and subspace diagonalization. The latter two are the bottlenecks which have  $O(N^3)$  scaling. In the Gram-Schmidt routine in our RSDFT code, most of the computations are performed as matrix-by-matrix product, so that the computational performance has reached 80–90% of the theoretical peak performance by using level 3 of Basic Linear Algebra Subprograms (BLAS). Similar techniques have been applied to the matrix construction and the wave function update in the subspace diagonalization routine. The diagonalization of subspace Hamiltonian is also performed in parallel by using ScaLAPACK or similar libraries.

Parallelization is performed by dividing the unit cell into several subregions, and each region is allocated on each CPU or compute node. Internode communication is performed by using the Message-Passing Interface (MPI) library. All of the computation is done in real-space. Global reduction communications occur in the computation of inner products of wave functions. This communication becomes time consuming as the number of nodes in parallel computations increases. In this case, we divide the compute nodes into several small groups and perform band-index parallelization by using these groups. Consequently, the number of nodes for grid-point parallelization is reduced and the cost of communication for global summation is also reduced.

In each node, we further parallelize the computation into several threads by using OpenMP directives. With this MPI and OpenMP hybrid parallelization scheme, we have performed self-consistent calculations of tens-of-thousands-of-atom systems, and also performed a benchmark test for 100 000-atom system with more than 640 000 cores at K computer. We have achieved extremely high performance even with such large number of CPU cores, and recorded more than three PFLOPS in effective performance. For this high performance, the RSDFT code was awarded the ACM Gordon-Bell prize for peak performance in 2011 [22].

In the actual calculations for twisted bilayer graphenes, we use a repeated slab model in which a bilayer graphene is separated from its images by a vacuum region with a thickness of more than 7 Å. The periodicity  $L_{\text{cell}}$  in the lateral plane depends on the twist angle  $\theta$  (see Appendix B and Table I). We have carefully examined the accuracy of our computations and found that the intergrid distance of 0.18 Å for structural optimizations suffices to guarantee the total energy with an error less than 0.1 meV/atom, and that the distance of 0.31 Å for the band-structure calculations does to guarantee the KS energy level with an error less than 1 meV. Geometry optimization has been performed until the remaining force on each atom becomes less than 0.5 meV/Å. Structures for  $\theta < 2^\circ$  are constructed by extrapolating the fully optimized structures for larger  $\theta$ , as is explained in Appendix D. A commensurate (see Appendix B) tBLG with  $\theta = 0.76^\circ$  includes 22 708 atoms in the unit cell, which is the largest system calculated in the present paper.

#### APPENDIX B: COMMENSURATE TWISTED BILAYER GRAPHENE

A twisted bilayer graphene (tBLG) is obtained by stacking two graphene layers with a twist angle  $\theta$ . In the directions

TABLE I. A list of tBLGs calculated in this work. For  $\theta < 2^\circ$ , atomic structures are obtained by extrapolating the fully optimized geometries of the tBLGs with larger  $\theta$  (see Appendix D).

$(M, N)$	$\theta$ (twist angle)[ $^\circ$ ]	$L_{\text{cell}}$ (cell size) [Å]	$N_{\text{atom}}$ [/cell]
(44,43)	0.76	184.01	22 708
(38,37)	0.88	158.63	16 876
(34,33)	0.99	141.71	13 468
(32,31)	1.05	133.25	11 908
(31,30)	1.08	129.02	11 164
(30,29)	1.12	124.79	10 444
(29,28)	1.16	120.56	9748
(28,27)	1.20	116.33	9076
(23,22)	1.47	95.18	6076
(18,17)	1.89	74.04	3676
(12,11)	2.88	48.66	1588
(9,8)	3.89	35.98	868
(8,7)	4.41	31.75	676
(7,6)	5.09	27.52	508
(6,5)	6.01	23.30	364
(5,4)	7.34	19.07	244
(9,7)	8.26	33.93	772
(4,3)	9.43	14.86	148
(8,6)	9.43	29.71	592
(7,5)	10.99	25.50	436
(3,2)	13.17	10.65	76
(6,4)	13.17	21.29	304
(9,6)	13.17	31.94	684
(8,5)	15.18	27.74	516
(5,3)	16.43	17.10	196
(7,4)	17.90	23.55	372
(9,5)	18.73	30.01	604
(2,1)	21.79	6.46	28
(4,2)	21.79	12.92	112
(6,3)	21.79	19.38	252
(8,4)	21.79	25.85	448
(10,5)	21.79	32.31	700
(9,4)	25.04	28.16	532
(7,3)	26.01	21.71	316
(5,2)	27.80	15.25	156
(10,4)	27.80	30.50	624
(8,3)	29.41	24.05	388
(11,4)	30.16	32.86	724
(3,1)	32.20	8.81	52
(6,2)	32.20	17.61	208
(9,3)	32.20	26.42	468
(10,3)	34.54	28.79	556
(7,2)	35.57	19.99	268
(11,3)	36.52	31.18	652
(4,1)	38.21	11.19	84
(8,2)	38.21	22.38	336
(9,2)	40.35	24.79	412
(5,1)	42.10	13.60	124
(10,2)	42.10	27.20	496
(11,2)	43.57	29.61	588
(6,1)	44.82	16.01	172
(12,2)	44.82	32.03	688
(7,1)	46.83	18.44	228
(8,1)	48.36	20.87	292
(9,1)	49.58	23.30	364
(10,1)	50.57	25.73	444
(11,1)	51.39	28.16	532
(12,1)	52.07	30.06	628

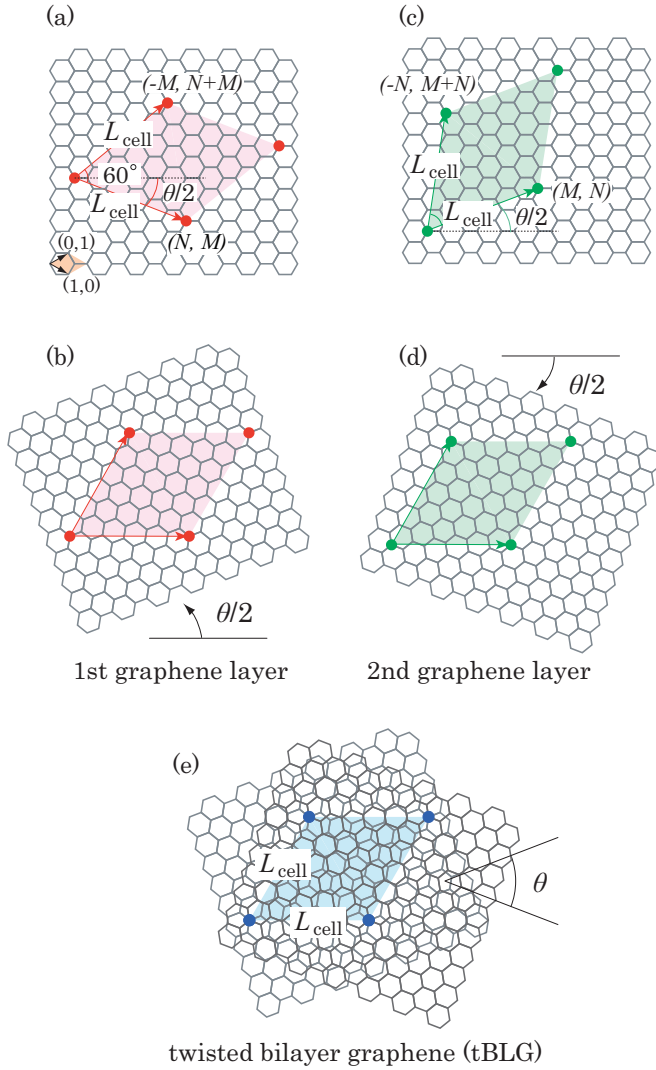


FIG. 6. (Color online) The unit cell of a commensurate  $(M, N)$  tBLG. Suppose a graphene sheet with a superperiodicity defined by the two  $(N, M)$  and  $(-M, N + M)$  vectors (a) and rotate it by  $+\theta/2$  (b). Similarly, take a graphene sheet with periodicity defined by the  $(M, N)$  and  $(-N, M + N)$  vectors (c) and rotate it by  $-\theta/2$  (d). The commensurate tBLG (e) with the twist angle  $\theta$  and the periodicity  $L_{\text{cell}}$  is obtained by stacking the thus obtained two layers, (b) and (d).

parallel to the layers, the atomic arrangements have periodicity only for particular values of the twist angle  $\theta$ . Our calculations are performed for such tBLGs where the periodicities of the two layers are commensurate to each other (commensurate tBLG). We choose a lateral position at which two A-site atoms on the different layers share the position, and set the twist axis penetrating through the two atoms. Shift of the twist axis from the A sites generates essentially identical tBLG structures. Due to the  $C_3$  symmetry of the graphene layers, commensurate tBLGs are of hexagonal symmetry, and are labeled by a pair of integers  $(M, N)$  as explained below.

Figure 6(e) shows the unit cell of a commensurate tBLG labeled by  $(M, N)$ . This tBLG is obtained by stacking two graphene layers shown in Figs. 6(b) and 6(d). The former is a graphene layer with the superperiodicity defined by  $(N, M)$

and  $(-M, N + M)$  vectors [Fig. 6(a)], followed by the twist rotation with  $+\theta/2$  [Fig. 6(b)]. The latter is a layer with the superperiodicity defined by  $(M, N)$  and  $(-N, M + N)$  vectors [Fig. 6(c)], followed by the rotation with  $-\theta/2$  [Fig. 6(d)]. Any commensurate tBLG is labeled by this  $(M, N)$  index. The  $(M, N)$  index for the commensurate tBLG is related with the twist angle  $\theta$ , the cell size  $L_{\text{cell}}$ , and the number of atoms  $N_{\text{atom}}$  in the unit cell as

$$\cos \theta = \frac{N^2 + 4NM + M^2}{2(N^2 + NM + M^2)}, \quad (\text{B1})$$

$$L_{\text{cell}} = d\sqrt{3(N^2 + NM + M^2)}, \quad (\text{B2})$$

$$N_{\text{atom}} = 4(N^2 + NM + M^2), \quad (\text{B3})$$

where  $d$  is the C-C distance in the graphene layer. The commensurate  $(M, N)$  tBLGs we have calculated in this work are summarized in Table I.

The reciprocal space of commensurate tBLG is also of hexagonal symmetry. The center and apex of the Brillouin zone (BZ) are labeled as  $\Gamma$  and K ( $K'$ ), respectively. In Fig. 3, we have drawn the band structures of the tBLGs along the  $\Gamma K$  line in the corresponding BZ.

### APPENDIX C: MOIRÉ PATTERN AND THE EXTENT OF THE AA STACKING REGION

A tBLG with  $\theta + 120^\circ$  is identical with that with  $\theta$  due to the  $C_3$  symmetry. A tBLG with  $-\theta$  is also a mirror image of the tBLG with  $\theta$ . Hence, we confine ourselves to the range of  $0^\circ < \theta < 60^\circ$ . Figure 7 is a schematic view of tBLG drawn for several twist angles. We find that the patterns are qualitatively different for  $20^\circ < \theta < 40^\circ$  [Figs. 7(d)–7(h)] and for the other angles [Figs. 7(a)–7(c) and 7(i)–7(k)]: In the latter, we find a periodic and hexagonal patchwork of the AA, the AB, and other stacking regions, which we call Moiré pattern; in the former, we do not find it. The atomic structure for  $60^\circ - \theta$  is obtained from that for  $\theta$ , by laterally translating one graphene layer with respect to the other after a mirror inversion of the bilayer. The Moiré patterns are essentially the same for the tBLG with  $60^\circ - \theta$  and that with  $\theta$ , as we find in Fig. 7.

In Fig. 7(a), we show the period  $L$  of the Moiré pattern, i.e., the distance between two neighboring AA stacking regions, by an arrow. As shown in Fig. 7, this period  $L$  and size of each AA, AB, and other stacking regions become larger as the twist angle  $\theta$  becomes closer to either  $0^\circ$  or  $60^\circ$ . The period  $L$  is given by

$$L = \frac{\sqrt{3}d}{2 \sin\left(\frac{\theta}{2}\right)} \quad (\text{C1})$$

for  $\theta$  close to  $0^\circ$ . Even in the incommensurate (nonperiodic) tBLGs, the Moiré pattern shows certain periodicity. For commensurate  $(M, N)$  tBLGs with small  $\theta$ , the Moiré period  $L$  and the cell size  $L_{\text{cell}}$  have a relation of

$$L = \frac{L_{\text{cell}}}{|M - N|} \quad (\text{C2})$$

as derived from Eqs. (B1), (B2), and (C1). For example,  $L = L_{\text{cell}}/2$  and  $L = L_{\text{cell}}$  for (9,7) [ $\theta = 8.26^\circ$ ] and (9,8) [ $\theta = 3.89^\circ$ ] tBLGs, respectively. This is what we actually find in Figs. 1(b) and 1(c).

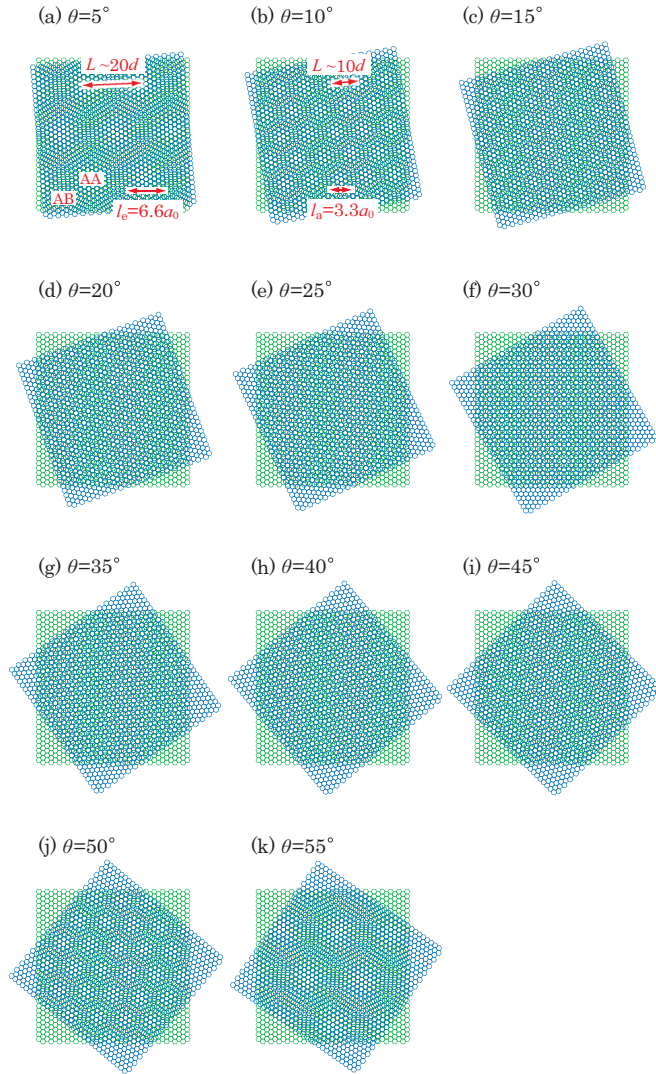


FIG. 7. (Color online) Moiré patterns in tBLGs schematically drawn for the twist angle  $\theta$  of (a)  $5^\circ$ , (b)  $10^\circ$ , (c)  $15^\circ$ , (d)  $20^\circ$ , (e)  $25^\circ$ , (f)  $30^\circ$ , (g)  $35^\circ$ , (h)  $40^\circ$ , (i)  $45^\circ$ , (j)  $50^\circ$ , and (k)  $55^\circ$ . The pattern for the tBLG with  $60^\circ - \theta$  is essentially the same as that with  $\theta$ .

As stated in our paper, there are two critical angles,  $\theta_a \sim 10^\circ$  and  $\theta_e \sim 5^\circ$ , below which the graphene layers are corrugated and the Fermi velocity is drastically reduced, respectively. Since the area of the particular stacking region, e.g., the AA stacking region, increases with the decreasing  $\theta$ , the critical angle corresponds to the critical area where the stacking is recognized to be AA. The linear dimension of the critical area  $l_0$  which corresponds to the critical angle  $\theta_0$  is simply estimated as follows.

The lateral point separated by  $l_0/2$  from the twist-axis point is shifted by  $l_0\theta/2$  by the rotation of  $\theta$ . When this shift is more than half of the in-plane atomic distance  $d/2$ , the stacking around the lateral point is no longer the same stacking near the twist-axis point [36]. The condition that two lateral points separated by  $l_0$  have the same stacking is therefore

$$\frac{l_0\theta}{2} \leq \frac{d}{2}. \quad (\text{C3})$$

The linear dimension  $l_0$  derived by taking the equal sign of Eq. (C3) with the critical angle  $\theta_0$  is thus the dimension representing the extent of the critical area:

$$l_0 = \frac{d}{\theta_0}. \quad (\text{C4})$$

Then we obtain  $l_a \sim 3.3a_0$  for  $\theta_a = 10^\circ$  and  $l_e \sim 6.6a_0$  for  $\theta_e = 5^\circ$ , where  $a_0 = \sqrt{3}d$  is the lattice constant of the honeycomb lattice of graphene. We thus argue that the valence electron density senses the AA stacking region, in other words the Moiré pattern, when the linear dimension of the critical area is larger than  $3.3a_0$ , whereas the more extended particular electron state near the Fermi level requires the wider area with the linear dimension at least  $6.6a_0$  to sense the AA stacking region.

#### APPENDIX D: EXTRAPOLATION OF ATOMIC STRUCTURES FOR SMALL TWIST ANGLES

Computational cost of structural optimization rapidly increases as the number of atoms in the unit cell becomes large. In this work, atomic structures of tBLGs with  $\theta > 2^\circ$  are obtained by performing full structural optimizations, whereas for tBLGs with  $\theta < 2^\circ$  with the index of  $(N, N-1)$ , which have more than  $\sim 3,000$  atoms/cell, structures are obtained by extrapolating the optimized geometries for  $\theta > 2^\circ$  as is explained below.

As we have shown in the paper, the stacking pattern of the layers decides their corrugations in the optimized structures. Stacking patterns in the unit cells for all  $(N, N-1)$  tBLGs are qualitatively similar: an AA stacking region and two AB stacking regions are in the unit cell. This leads to qualitatively similar corrugations of the layers in the cells as we find, for example, in Figs. 8(a) and 8(b), which are the optimized structures for  $(N, N-1)$  tBLGs with  $\theta = 6.01^\circ$  ( $N = 6$ ) and  $\theta = 3.89^\circ$  ( $N = 9$ ), respectively. We thus reasonably obtain the corrugated structure for  $(N, N-1)$  tBLGs with  $\theta < 2^\circ$  by extrapolating the structures computed for  $\theta > 2^\circ$ . Such extrapolation is conveniently done in the reciprocal space as follows. We optimize the structures of tBLGs with relatively large twist angles. The vertical coordinate  $z$  as a function of the lateral coordinate  $\mathbf{r} = (x, y)$  is obtained for each atom in the tBLG:  $z(x, y) = z(\mathbf{r})$ . This is Fourier-expanded by using the two-dimensional reciprocal lattice vectors  $\mathbf{G}_j$  in the lateral cell:

$$z(\mathbf{r}) = \sum_{j=0}^{\infty} \{\alpha_j \cos(\mathbf{G}_j \mathbf{r}) + \beta_j \sin(\mathbf{G}_j \mathbf{r})\}. \quad (\text{D1})$$

The Fourier coefficients  $\{\alpha_j, \beta_j\}$  are computed for the fully optimized structures of  $(N, N-1)$  tBLGs with larger  $\theta$ . In Fig. 8(d), the calculated Fourier coefficient  $\alpha_1$ , corresponding to the shortest nonzero reciprocal vector  $\mathbf{G}_1$ , is plotted as a function of  $\theta$ . We have found that the calculated data are well fitted by a Gaussian function shown by the solid curve in Fig. 8(d). This fitting provides the Fourier coefficients for  $(N, N-1)$  tBLGs with smaller  $\theta$ . Other Fourier coefficients are also extrapolated in this way. Figure 8(c) shows the corrugated atomic structure of the  $(34, 33)$

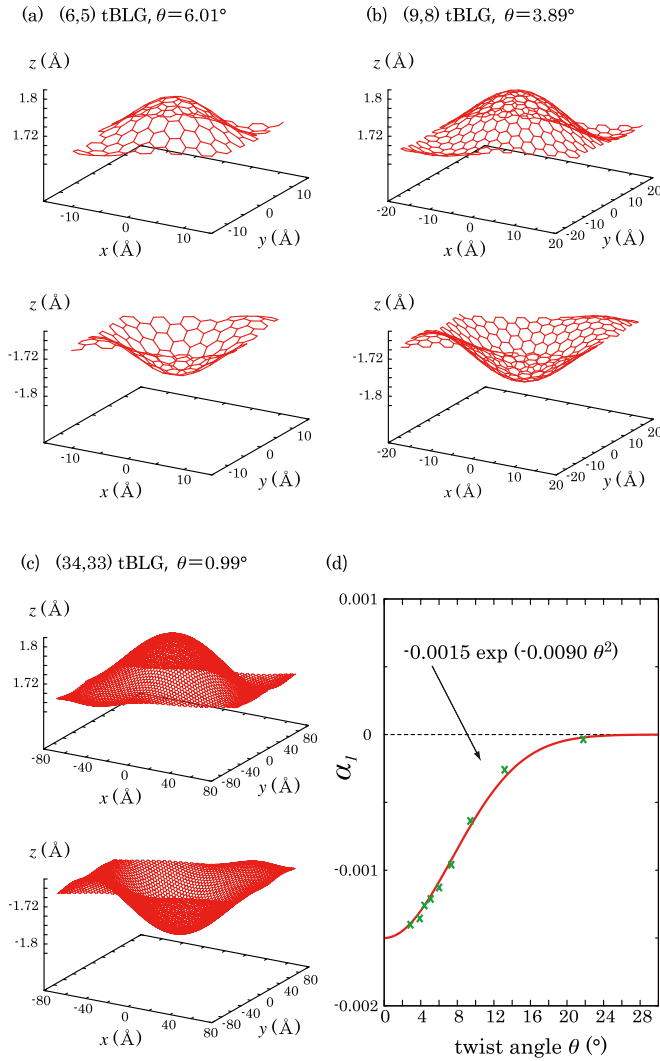


FIG. 8. (Color online) Atomic structures of  $(N, N - 1)$  tBLGs with the twist angle  $\theta$  of (a)  $6.01^\circ$  ( $N = 6$ ), (b)  $3.89^\circ$  ( $N = 9$ ), and (c)  $0.99^\circ$  ( $N = 34$ ). The structures are obtained by full structural optimizations for (a) and (b). The structure in (c) is obtained by the extrapolation (see Appendix D). (d) A Fourier coefficient  $\alpha_1$  [Eq. (D1)] is calculated as a function of  $\theta$ , being fitted by the solid curve for extrapolation to the smaller twist angle ( $\theta < 2^\circ$ ).

tBLG ( $\theta = 0.99^\circ$ ,  $N = 34$ ), which is constructed by using the extrapolated Fourier coefficients. The cosine coefficients for the 7 shortest reciprocal vectors (including  $\mathbf{G}_0 = \mathbf{0}$ ) are found to be dominant, and the other coefficients are safely negligible.

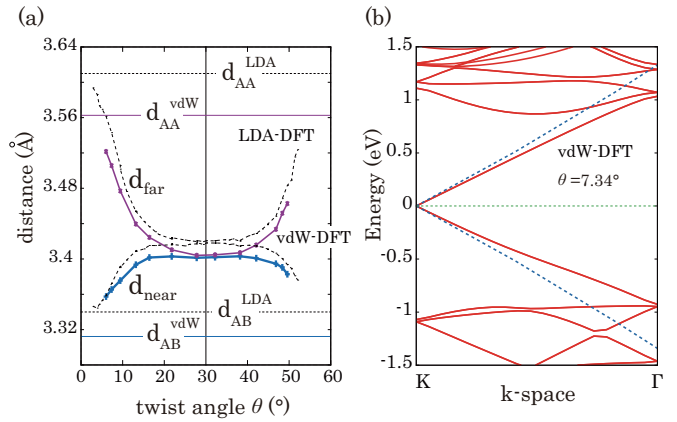


FIG. 9. (Color online) (a) The farthest distance  $d_{\text{far}}$  and the nearest distances  $d_{\text{near}}$  between the graphene layers in tBLGs, as functions of the twist angle  $\theta$ . The solid and dashed lines are from vdW-DFT and LDA-DFT calculations, respectively. The interlayer distances of purely AA or AB stacking bilayers are also shown by horizontal lines. (b) The band dispersions of a tBLG with  $\theta = 7.34^\circ$ , obtained by vdW-DFT. The dashed line is the corresponding dispersion of the SLG. The Fermi levels are set to be 0.

#### APPENDIX E: VAN DER WAALS CALCULATION

To verify the validity of LDA, we here show the results with a more sophisticated functional, vdW-DFT [27,37], that is capable of treating the van-der Waals interactions between the graphene layers. Calculations have been performed using the VASP code [38]. Projector-augmented wave (PAW) potential [39], and a plane-wave basis set with the cutoff energy of 400 eV are used.

Figure 9(a) shows the farthest and nearest distances,  $d_{\text{far}}$  and  $d_{\text{near}}$ , of the layers in tBLGs as functions of the twist angle  $\theta$ . Solid and dashed lines correspond to the LDA and vdW calculations, respectively. We find that the results are essentially the same between them: the layers are flat for  $\theta \sim 30^\circ$ , and are corrugated for  $\theta < \sim 10^\circ$  and  $\theta > \sim 50^\circ$ . The reason why the corrugations are quantitatively different between the schemes is ascribed to the difference in the interlayer distance for the nontwisted bilayer between the schemes:  $d_{\text{AA}} = 3.56 \text{ \AA}$  (vdW-DFT) and  $3.61 \text{ \AA}$  (LDA);  $d_{\text{AB}} = 3.31 \text{ \AA}$  (vdW-DFT) and  $3.34 \text{ \AA}$  (LDA).

Figure 9(b) shows the band structure of a tBLG with  $\theta = 7.34^\circ$ . The Dirac cone of the single-layer graphene (SLG) is also shown by a dashed line. We find that the Fermi velocity in the tBLG is reduced compared with that in SLG,  $v_{\text{F}}^0$ , which is also the same result as the LDA calculation. The reduction rate ( $v_{\text{F}}/v_{\text{F}}^0$ ) is calculated to be 0.89 and 0.93 for vdW-DFT and LDA, respectively. The above shows that our conclusions of the paper are unchanged even if vdW-DFT is used.

[1] W. T. Pong and C. Durkan, *J. Phys. D* **38**, R329 (2005).  
 [2] Z. Y. Rong and P. Kuiper, *Phys. Rev. B* **48**, 17427 (1993).  
 [3] A. H. Macdonald and R. Bistritzer, *Nature (London)* **474**, 453 (2011).

[4] Z. Ni, Y. Wang, T. Yu, Y. You, and Z. Shen, *Phys. Rev. B* **77**, 235403 (2008).  
 [5] P. Poncharal, A. Ayari, T. Michel, and J.-L. Sauvajol, *Phys. Rev. B* **78**, 113407 (2008).

- [6] J. Hass, F. Varchon, J. E. Millan-Otoya, M. Sprinkle, N. Sharma, W. A. de Heer, C. Berger, P. N. First, L. Magaud, and E. H. Conrad, *Phys. Rev. Lett.* **100**, 125504 (2008).
- [7] F. Varchon, P. Mallet, L. Magaud, and J.-Y. Veuillen, *Phys. Rev. B* **77**, 165415 (2008).
- [8] A. Luican, Guohong Li, A. Reina, J. Kong, R. R. Nair, K. S. Novoselov, A. K. Geim, and E. Y. Andrei, *Phys. Rev. Lett.* **106**, 126802 (2011).
- [9] T. Ohta, J. T. Robinson, P. J. Feibelman, A. Bostwick, E. Rotenberg, and T. E. Beechem, *Phys. Rev. Lett.* **109**, 186807 (2012).
- [10] J. Hicks, M. Sprinkle, K. Shepperd, F. Wang, A. Tejada, A. Taleb-Ibrahimi, F. Bertran, P. Le Fèvre, W. A. de Heer, C. Berger, and E. H. Conrad, *Phys. Rev. B* **83**, 205403 (2011).
- [11] J. C. Slonczewski and P. R. Weiss, *Phys. Rev.* **109**, 272 (1958).
- [12] K. S. Novoselov, A. K. Geim, S. V. Morozov, D. Jiang, M. L. Katsnelson, I. V. Grigorieva, S. V. Dubonos, and A. A. Firsov, *Nature (London)* **438**, 197 (2005).
- [13] M. Sprinkle, D. Siégel, Y. Hu, J. Hicks, A. Tejada, A. Taleb-Ibrahimi, P. Le Fèvre, F. Bertran, S. Vizzini, H. Enriquez, S. Chiang, P. Soukiassian, C. Berger, W. A. de Heer, A. Lanzara, and E. H. Conrad, *Phys. Rev. Lett.* **103**, 226803 (2009).
- [14] S. Latil, V. Meunier, and L. Henrard, *Phys. Rev. B* **76**, 201402(R) (2007).
- [15] S. Shallcross, S. Sharma, and O. A. Pankratov, *Phys. Rev. Lett.* **101**, 056803 (2008).
- [16] J. M. B. Lopes dos Santos, N. M. R. Peres, and A. H. Castro Neto, *Phys. Rev. Lett.* **99**, 256802 (2007).
- [17] S. Shallcross, S. Sharma, E. Kandelaki, and O. A. Pankratov, *Phys. Rev. B* **81**, 165105 (2010).
- [18] G. Trambly de Laissardière, D. Mayou, and L. Magaud, *Nano Lett.* **10**, 804 (2010).
- [19] E. Suárez Morell, J. D. Correa, P. Vargas, M. Pacheco, and Z. Barticevic, *Phys. Rev. B* **82**, 121407(R) (2010).
- [20] R. Bistritzer and A. H. MacDonald, *PNAS* **108**, 12237 (2011).
- [21] J.-I. Iwata, D. Takahashi, A. Oshiyama, B. Boku, K. Shiraishi, S. Okada, and K. Yabana, *J. Comput. Phys.* **229**, 2339 (2010).
- [22] Y. Hasegawa, J.-I. Iwata, M. Tsuji, D. Takahashi, A. Oshiyama, K. Minami, T. Boku, F. Shoji, A. Uno, M. Kurokawa, H. Inoue, I. Miyoshi, and M. Yokokawa, *Proceedings of 2011 International Conference for High Performance Computing, Networking, Storage and Analysis (SC11), Seattle, USA* (ACM, New York, NY, 2011), Article No. 1.
- [23] P. Hohenberg and W. Kohn, *Phys. Rev.* **136**, B864 (1964).
- [24] W. Kohn and L. J. Sham, *Phys. Rev.* **140**, A1133 (1965).
- [25] J. P. Perdew and A. Zunger, *Phys. Rev. B* **23**, 5048 (1981).
- [26] D. Vanderbilt, *Phys. Rev. B* **41**, 7892 (1990).
- [27] M. Dion, H. Rydberg, E. Schröder, D. C. Langreth, and B. I. Lundqvist, *Phys. Rev. Lett.* **92**, 246401 (2004).
- [28] J. Berashevich and T. Chakraborty, *Phys. Rev. B* **84**, 033403 (2011).
- [29] B. Liu, M.-F. Yu, and Y. Huang, *Phys. Rev. B* **70**, 161402(R) (2004).
- [30] G. Trambly de Laissardière, D. Mayou, and L. Magaud, *Phys. Rev. B* **86**, 125413 (2012).
- [31] W. Kohn, *Phys. Rev. Lett.* **76**, 3168 (1996).
- [32] <http://www.top500.org/>
- [33] J. R. Chelikowsky, N. Troullier, and Y. Saad, *Phys. Rev. Lett.* **72**, 1240 (1994).
- [34] J.-I. Iwata, K. Shiraishi, and A. Oshiyama, *Phys. Rev. B* **77**, 115208 (2008).
- [35] Y. Hasegawa, J.-I. Iwata, M. Tsuji, D. Takahashi, A. Oshiyama, K. Minami, T. Boku, H. Inoue, Y. Kitazawa, I. Miyoshi, and M. Yokokawa, *Int. J. High Perform. C.* **28**, 335 (2014).
- [36] The AB stacking is obtained from the AA stacking, by translating one layer with respect to the other by  $d$ . Thus, relative displacement of the layers to change the stacking is roughly estimated to be  $\sim d$ .
- [37] J. Klimes, D. R. Bowler, and A. Michaelides, *Phys. Rev. B* **83**, 195131 (2011): The optB86b is used in the present calculation.
- [38] G. Kresse and J. Furthmüller, *Phys. Rev. B* **54**, 11169 (1996).
- [39] P. E. Blöchl, *Phys. Rev. B* **50**, 17953 (1994).